Tunable magnetism and structural transformations in mixed light- and heavy-lanthanide dialuminides

Arjun K. Pathak, D. Paudyal, Y. Mudryk, K. A. Gschneidner, Jr., and V. K. Pecharsky

Tunable magnetism and structural transformations in mixed light and heavy-lanthanide dialumindes

Arjun K. Pathak, [1,a] D. Paudyal,[1] Y. Mudryk,[1] K. A. Gschneidner, Jr.,[1,2, b] and V. K. Pecharsky[1,2]

[1]*The Ames Laboratory, U.S. Department of Energy, Iowa State University, Ames, Iowa 50011, USA*

[2]*Department of Materials Science and Engineering, Iowa State University, Ames, Iowa 50011, USA*

Rare earth intermetallics play a critical yet often obscure role in numerous technological applications, including sensors, actuators, permanent magnets, and rechargeable batteries; therefore, understanding their basic science is of utmost importance. Here we report structural behaviors, specific heat, and magnetism of $Pr_{1-x}Er_xAl_2$ studied by means of temperature-dependent x-ray powder diffraction, heat capacity and magnetization measurements, in addition to first principles calculations. Although the cubic lattice of $PrAl_2$ distorts tetragonally at the Curie temperature, T_C, it the distortion is rhombohedral in $ErAl_2$, creating a potential for instability in the pseudo-binary $PrAl_2 - ErAl_2$ system. When $0.05 \leq x \leq 0.5$, materials show complex magnetization behaviors, including metamagnetic transitions and Griffith-like phase. Unique among other mixed lanthanide dialumindes, the substitution of Er for Pr in $Pr_{1-x}Er_xAl_2$ results in unexpected ferrimagnetic behavior, and the ferrimagnetic interactions become strongest around x = 0.25, where the compound shows unusual metamagnetic-like transitions observed only in

---

[a] corresponding author: pathak138@ameslab.gov

[b] Deceased

the odd-numbered quadrants of the full magnetic field cycles. The electronic structure calculations, including exchange interactions and crystal field splitting, magnetic moments, anisotropic $4f$ energy density, and magnetic surface potentials rationalize the interesting physics observed experimentally.

I. Introduction

Tuning the chemistry of materials often leads to discovery of exotic phenomena that both expand basic science and find applications in novel technologies. For example, when a material shows an extraordinarily strong responsiveness to external stimuli, such as temperature, pressure, and magnetic field, such behavior warrants an inquiry from both basic and applied science to understand and then adjust up or down as needed. Responsive materials often exhibit field-induced first order structural or magnetic phase transformations and metamagnetism, and find practical applications based on very strong (a.k.a. giant or colossal) magnetoresistive, magnetocaloric and magnetostrictive effects [1,2,3,4].

Among several families of materials that show strong responsiveness to external stimuli are rare earth (R) dialumindes, RAl_2, which have been known for decades, but much of fascinating basic science is only beginning to come to light [5,6]. For example, a recent study found an anomalous heat capacity behavior in $PrAl_2$ below 2 K. Further, $PrAl_2$ exhibits a cubic to tetragonal polymorphic transformation at the ferromagnetic (FM)-paramagnetic (PM) transition ($T_C \approx 30$ K) in a zero magnetic field but the compound recovers the cubic symmetry under modest magnetic field H $\geq$ 10 kOe [7]. This

2

interesting sensitivity of the crystal lattice to applied magnetic field arises from the interplay between localized (4f) and a delocalized (spd) electronic states.

Mixing one lanthanide (R) with another (R') in pseudobinary compounds such as $Er_{1-x}Dy_x$, $Er_{1-x}Dy_xAl_2$, $Er_{1-x}Tb_xAl_2$, and $Tm_{1-x}Tb_xAl_2$ [8,9,10,11] results in unusual low temperature anomalies in heat capacity and multiple ordering phenomena. In some cases, additional first order transitions are observed below the main FM-PM transition at T_C. So far this was observed only for certain critical concentrations of R', around $x = 0.25$, when both R and R' are heavy lanthanides. The observed first order transitions generally weaken with field and no field induced anomalies are seen for H $\geq$ 10 kOe. The unusual physics is due to the competing influences of exchange interactions, crystalline electric field splitting, and magnetoelasticity, as well as quadrupolar and higher order effects. In particular, our earlier calculations show that the average quadrupolar moment is near zero at x $\cong$ 0.25; for example, quadrupolar moment changes from positive to negative in $Er_{1-x}Dy_xAl_2$ when x = 0.25 [12], and this leads to a low temperature anomaly in heat capacity.

Even more complex magnetic behavior can be expected when combining light and heavy lanthanides in rare earth dialuminides. According to Hund's rule, the 4f orbital and spin moments are antiparallel in light (e.g. Pr) yet they are parallel in heavy (e.g. Er) lanthanides, and the competition between different single-ion anisotropies of Pr and Er ions coupled with nearest-neighbor and next-neighbor exchange interactions may lead to unusual behaviors. Indeed we have observed some fundamentally new and interesting

3

phenomena when combining heavy R with light R' [13]. However, the so-called magic concentration 'x = 0.25' for mixed heavy and heavy lanthanides does not apply for a mixture of light and heavy lanthanides where the higher order terms, namely quadrupolar and octupolar moment contributions are also playing a role [13]. Therefore, it is important to explore the whole $Pr_{1-x}Er_xAl_2$ pseudobinary system and carry out the magnetic, heat capacity, and structural investigation in order to establish, if any, its own magic composition. Here, we present the effect of compositional variations on the low temperature crystal structure, Schottky specific heat, and magnetic properties of $Pr_{1-x}Er_xAl_2$ compounds. First principle calculations have also been performed to shed light and understand the ground state magnetism and crystal structures of $Pr_{1-x}Er_xAl_2$.

II. Experimental and computational details

Polycrystalline $Pr_{1-x}Er_xAl_2$ samples with $0 \leq x \leq 1$ were prepared by arc melting stoichiometric amounts of the constituent elements in an argon atmosphere. The Pr and Er metals were obtained from the Materials Preparation Center of the Ames Laboratory and were, respectively, 99.98+ wt% (99.85+ at. %), and 99.98+ wt% (99.82+ at. %) pure with regard to all other elements in the periodic table [14]. The Al metal of 4N purity was purchased from Alfa Aeser Inc.

The crystal structure was determined by x-ray powder diffraction (XRD) experiments performed between room temperature and 5 K in zero and applied magnetic fields up to 30 kOe using the Rigaku rotating anode diffractometer (TTRAX system, Mo Kα

4

radiation) equipped by a continuous flow cryostat and a split-coil superconducting magnet [15]. The room temperature XRD measurements confirm that all $Pr_{1-x}Er_xAl_2$ alloys crystallize in the $MgCu_2$ type cubic Laves-phase structure with no detectable secondary phases (Fig. 1). The structural parameters were determined by Rietveld analysis using LHPM Rietica [16]. The dc magnetization was measured in a Quantum Design superconducting quantum interference device (MPMS-XL7 magnetometer) and a physical property measurement system (PPMS) by using the vibrating sample magnetometer in magnetic fields up to 140 kOe. The heat capacity measurements were performed using a homemade adiabatic heat-pulse calorimeter [17] in applied magnetic fields up to 100 kOe.

The local spin density approximation including Hubbard U (LSDA+U) [18] approach has been employed to investigate the electronic structure and magnetism of $Pr_{1-x}Er_xAl_2$ compounds. The LSDA+U calculations have been performed within the tight binding linear muffin tin orbital (TB-LMTO) [19] and full potential linear augmented plane wave (FP-LAPW) [20] methods. To model the statistical distribution of Er and Pr atoms in the lattice, the cubic symmetry was converted to the triclinic (P1) symmetry. Depending upon the concentration, the Pr and Er atoms were randomly distributed among 8 independent rare earth atom positions available inside the pseudocubic triclinic unit cell with $a = b = c$ and $\alpha = \beta = \gamma = 90°$ of the same volume as the original cubic unit cell, thus easily modeling any of the seven intermediate concentrations with x = 0.125, 0.250, 0.375, 0.5, 0.625, 0.75 and 0.875. The orbital dependent Coulomb and exchange interactions in LSDA+U remove the degeneracy, and the 4f states split as prescribed by

5

the tetrahedral site symmetry of R atoms, octahedral local symmetry of Al atoms, and the number of partially filled orbitals in both spin channels obeying the Hund's spin and orbital rules in the Laves-phase structure of these compounds. The electronic structure calculations performed with different values of Hubbard U ranging from 1 eV to 7 eV indicate that with the higher values of the U, the spin up $4f$ states are shifted to the lower energy while the spin down $4f$ states are shifted to the higher energy, as expected. The k-space integrations have been performed with $16 \times 16 \times 16$ Brillouin zone mesh which was sufficient for convergence of total energies, magnetic moments, and $4f$ and $5d$ splitting.

III. Results and Discussion

The results of the heat capacity C_p measurements of $Pr_{1-x}Er_xAl_2$ alloys at zero magnetic field are shown in Fig. 2. The room temperature C_p value for all compounds is ~72 J mol^{-1} K^{-1}, approaching the classical Dulong and Petit limit of the lattice heat capacity at constant volume $C_V = 3nR = 74.83$ J mol^{-1} K^{-1}, where $n = 3$ is the number of atoms per formula unit and R is the universal gas constant [21]. The magnitudes of sharp λ-type anomalies in C_p observed at T_C gradually decrease upon increasing Er concentration when x ≤ 0.5 but when x = 0.95, where Er concentration is dominant, the anomaly broadens and regains magnitude. As shown in Fig. 2b, T_C of $Pr_{1-x}Er_xAl_2$ decreases almost linearly with Er concentration, suggesting decreasing strength of the exchange interactions with increase in x (Er) as confirmed from the theoretical calculations discussed below. Fig. 2c shows the magnetic contribution to the heat capacity (C_M) as a function of temperature estimated by subtracting the prorated heat capacities of

6

nonmagnetic $LaAl_2$ and $LuAl_2$ from the heat capacity of $Pr_{1-x}Er_xAl_2$, as described in Ref. [10]. The magnetic entropy (S_M) above T_C (at T = 100 K) is close to the theoretically expected $Rln(2J+1)$, for example it reaches 19 J $mol^{-1}K^{-1}$, i.e. 93% of the theoretical value for x = 0.4. S_M at T_C decreases with Er concentration up to x = 0.25 and then begins to increase with increasing Er concentration (Fig. 2d, inset), where ferrimagnetic interactions are the strongest as confirmed by electronic structure calculations.

Earlier we have observed that upon the application of magnetic field, C_p of $Pr_{0.6}Er_{0.4}Al_2$ shows an additional phase transition below T_C at $40 \leq H \leq 90$ kOe. In order to explore if similar behavior exists at other Er concentrations, we carried out heat capacity measurements in applied magnetic fields for $0 \leq x \leq 1$. Figure 3(a) shows the heat capacity behavior of $Pr_{0.9}Er_{0.1}Al_2$ in magnetic fields up to 50 kOe, which is typical for other measured alloys except for x = 0.25. The anomaly at T_C is suppressed and becomes broader when applied magnetic field is $H \geq 20$ kOe; no other anomalies have been observed for x = 0.05, 0.1, 0.5, 1 with the application of magnetic field up to 100 kOe. Interestingly, C_p for x = 0.25 (Fig. 3b) shows an additional field induced transition below T_C at T ~ 9 K (shown by a vertical arrow) at 25 kOe that shifts to lower temperature at H = 30 kOe and disappears at H > 40 kOe. Such anomalous behavior can be due to the competition between FIM and field induced FM phases where FIM interactions remain strong as suggested by theoretical calculations. It is observed that upturn in C_p at $T \leq 4$ K also decreases with the Er substitution compared to $PrAl_2$.

The low temperature C_p of $Pr_{0.9}Er_{0.1}Al_2$ was explored down to 0.4 K in magnetic fields up to 140 kOe (Fig. 4). The experimentally measured C_p at T ≤ 2 K was fitted using the following equation:

$$C_p = AT^3 + BT + C_N T^{-2} \tag{1}$$

where the first two terms are the standard lattice and electronic contributions, respectively, and the third accounts for the nuclear specific heat that arises due to the splitting of the nuclear hyperfine levels. Least squares fit yields $C_N = 650\pm3$ mJ K mol^{-1} which is lower than $C_N = 692\pm2$ mJ K mol^{-1} at H = 0 kOe for $PrAl_2$. Unlike in $PrAl_2$, which shows two linear dependencies of C_N, one for H ≤ 10 kOe, and another for H > 10 kOe, C_N for $Pr_{0.9}Er_{0.1}Al_2$ increases almost linearly with an external magnetic field. The difference in C_N behaviors in $PrAl_2$ and the Er-doped compound can be arising due to difference in magnetic ground states (discussed below). The maximum C_N of 700 mJ K mol^{-1} is observed at 140 kOe (inset, Fig. 4), which is also significantly lower than 1142 mJ K mol^{-1} for $PrAl_2$ [7]. Higher concentration of Er further suppresses the low temperature Schottky anomaly. For example, C_N becomes negligible for x = 0.95 [22]. According to first-principles calculations (below), the 5d exchange splitting decreases with Er doping and causing the decrease in the C_N (Fig. 10, below). The decrease in C_N with the substitution of Er in $PrAl_2$ may also occur due to lower crystalline electric field of Er compared to Pr.

The M(H) hysteresis loops for x = 0 and x = 0.95 at T = 2 K are shown in Fig. 5. Both alloys are ferromagnetic, and M(H) begins to saturate at H ≈ 10 kOe. $PrAl_2$ is a harder

8

ferromagnet compared to the $Pr_{0.05}Er_{0.95}Al_2$ (see insets in Fig. 5a-5b). Interesting features are observed in M(H) of $Pr_{1-x}Er_xAl_2$ for $0.05 \leq x \leq 0.5$. Figure 6 shows the M(H) hysteresis loops for x = 0.05, 0.1, 0.25 and 0.4. Magnetization for x = 0.05 and 0.1 (Fig. 6a-b) increases rapidly for H≤5 kOe then changes slowly at 5 kOe≤H≤40 kOe, and a shallow metamagnetic-like transition occurs above 40 kOe. The magnetization does not saturate even at magnetic field of 140 kOe, suggesting the dominant ferrimagnetic state where Pr and Er moments are non-collinear or antiparallel as expected from Hund's rule where the total angular momentum for Er is J = L+S, and for Pr, J = L-S.

M(H) data for x = 0.25 and x = 0.4 (Fig. 6c-d) show even more complex behavior at T = 2 K. For x = 0.25, several metamagnetic transitions are observed while magnetizing the sample, however magnetization M(H) changes smoothly during the demagnetizing process. For example, metamagnetic like steps in magnetization occur at approximately ±12 and ±46 kOe exclusively in the odd-numbered quadrants during two full magnetic field cycles (first, third, fifth, and seventh), while M(H) behavior is smooth in even-numbered quadrants, exhibiting unusual hysteresis between 25 kOe and 80 kOe. As shown in Fig. 6c, coercivity of 12 kOe is observed at 2 K. Such unusual evolution of the field-induced magnetization is likely related to different domain wall dynamics associated with the coexistence of different low field and high field magnetic phases. When x = 0.4, several consecutive metamagnetic transitions are observed at $|{\pm}61|$ kOe $\leq$ H $\leq |{\pm}115|$ kOe. Here the high-field multi-step metamagnetic transitions remain hysteretic, but are observed in the same quadrants. In both cases (x = 0.25, and 0.4), magnetization is not saturated even at 140 kOe, suggesting the dominance of FIM state.

The M(H) for x = 0.5 (not shown) is similar to the M(H) curve for x = 0.05 shown in Fig. 6a. Figs. 5 and 6 show that anomalous magnetic behaviors are observed for the samples with the intermediate concentration x, while at both ends of the pseudobinary $Pr_{1-x}Er_xAl_2$, the conventional FM behavior prevails.

The saturation magnetization (M_S) values estimated from the M vs. H^{-1} curves by extrapolating the curves to $H^{-1} = 0$ are 3.21, 3.22, 4.38, and 4.95 μ_B/f.u. for x = 0.05, 0.1, 0.25, and 0.4, respectively. These values are slightly below the calculated gJ values of 3.49, 4.23, 4.65, and 5.52 μ_B/f.u expected for the respective mixtures of Pr and Er. The crystal field effects is the most likely reason of low saturation magnetization.

The zero field cooled (ZFC), field cooled cooling (FCC), and field cooled warming (FCW) magnetization M(T) curves for x = 0 and 0.95 measured at 1 kOe are shown in Fig. 7. The Curie temperatures, T_C, obtained from M(T) data are 33 K and 14 K for x = 0 and 0.95, respectively, and are close to the values obtained from C_p data (Fig. 2b). The inverse dc susceptibilities (χ^{-1} = H/M), Fig. 7(b) and 7(d) for x = 0 and 0.95, respectively, follow the Curie-Weiss behavior. The effective magnetic moments, p_{eff}, and Weiss temperature, θ_p, are 3.36 μ_B/f.u. ($g[J(J+1)]^{1/2}$ = 3.58 μ_B) and 26 K, and 9.59 μ_B/f.u. ($g[J(J+1)]^{1/2}$ = 9.38 μ_B) and 21 K for x = 0 and 0.95, respectively. The positive θ_p values, that are close to T_C indicate the dominant FIM or FM interactions in these compositions, which is consistent with M(H) data.

The ZFC, FCC, and FCW M(T) curves for $0.1 \leq x \leq 0.5$ are quite different compared to x

= 0 and 0.95. Figure 8 shows a representative ZFC, FCC, and FCW M(T) data for x =

0.25 and 0.5 measured at 1 kOe. The ZFC and FCC M(T) data show irreversibility below

T_C. The χ^{-1} obtained from FCW data for $0.1 \leq x \leq 0.5$ also show anomalous behavior

above T_C. Similar to $Pr_{0.6}Er_{0.4}Al_2$ [13], two different temperature dependent regimes are

observed in $\chi^{-1}(T)$. At high temperatures (>50 K) it exhibits a typical Curie-Weiss

behavior but a sharp downturn is observed below a characteristic temperature, T_G, (insets,

Fig. 8b and 8d), signaling the onset of a Griffiths phase [23], which is characterized by

the short-range clustering and possible spin-fluctuations due to local chemical

inhomogenities in the distribution of Pr and Er atoms in the lattice. Similar behavior has

been observed in both localized 4f systems [23] and itinerant magnetic semiconductors

[24], but only in applied fields that are nearly two orders of magnitude lower ($0 \leq H \leq 20$

Oe). The p_{eff}, and θ_p for x = 0.25 and x = 0.5 are 5.68 μ_B/f.u. and 6 K, and 7.32 μ_B/f.u.

and 9.5 K, respectively. The observed p_{eff} are in excellent agreement with the expected

values of 5.71 and 7.24 μ_B/f.u. which is consistent with other RAl_2 systems where M_S is

significantly smaller, but p_{eff} is close to the theoretical values [25,11]. Significantly lower

values of θ_p ($\theta_p << T_C$) support the argument that FIM interactions are strong, if not

dominant for intermediate concentrations of Er in $Pr_{1-x}Er_xAl_2$.

Low temperature x-ray diffraction (LT-XRD) studies have been carried out for

$Pr_{1-x}Er_xAl_2$ with x = 0, 0.05, 0.1, 0.4, and 0.95, and 1. Similar to $PrAl_2$ [7], cubic to

tetragonal distortion has been observed for x = 0.05, and 0.1, except the extent of the

distortion decreases with Er concentration and even a small magnetic field can recover the cubic phase compared to that in PrAl$_2$ case (not shown). LT-XRD studies confirm no structural distortion for x = 0.4 [13]. Interestingly, LT-XRD results show that both Pr$_{0.05}$Er$_{0.95}$Al$_2$ and ErAl$_2$ have a structural transformation from the high-temperature cubic ($Fd\bar{3}m$) to the low-temperature rhombohedral ($R\bar{3}m$) phase at T$_C$. Figure 9a shows a contour plot of two high-angle Bragg reflections [(448) and (177)] of ErAl$_2$ showing their thermal evolution between 5 and 25 K and splitting at T$_C$. The cubic lattice distorts along the [111] direction, which we expect to be the easy magnetization axis for ErAl$_2$. As seen in Figure 9b the distortion is minor and without a notable discontinuity in the unit cell volume, in line with the second order nature of the transition. Comparison of ErAl$_2$ with ErCo$_2$ (both have the cubic C15 crystal structure at room temperature but the latter distorts rhombohedrally at T$_C$ with a sharp volume change and a first-order transition) indicates that in these intermetallic Laves phases the type of the distortion is defined by the rare-earth element, while the nature of the transition is defined by the presence of itinerant electron metamagnetism in ErCo$_2$ and its absence in ErAl$_2$. This argument can also be strengthened by taking the examples of DyAl$_2$ and DyCo$_2$ compounds where both distort tetragonally but the former has a second order and the latter undergoes a first order transition at their respective T$_C$'s.

IV. Theoretical Calculations

To understand the influence of crystal field (CF)-split 4f and 5d states on the evolution of magnetostructural transformations in Pr$_{1-x}$Er$_x$Al$_2$, we first analyze the density of states (DOS). The calculations show that the 4f CF splitting plays a key role in PM cubic to

FM tetragonal transformation in $PrAl_2$ [7]. When the Pr atoms are substituted by Er, additional split spin-up $4f$ states appear between -6 and -8 eV and additional split spin-down $4f$ states appear in two areas: between -5 and -6 eV and close to 2 eV. The split spin-up $4f$ states located close to the Fermi level, which are contributed by Pr form a gap (CF excitation gap associated with transitions between different $4f$ multiplets) with the split spin-down $4f$ states contributed by Er [13]. The gap itself is dependent on the electron-electron correlations, which are causing the change of the magnetic states via the admixing of the CF split states just above and below the Fermi level. Further, the degeneracy of the multiplets can be lifted by Zeeman interactions as a result of applying a magnetic field. Such degeneracy provides additional magnetic excitations associated with multiple magnetic transitions, which are indeed observed experimentally in $Pr_{1-x}Er_xAl_2$.

At high Er content the spin up $4f$ states close to the Fermi level are diminished and the physical behaviors resemble pure $ErAl_2$. Because of the tetrahedral and octahedral site symmetries of Er and Al atoms, respectively, there is $5d$ crystal field splitting in $ErAl_2$. This splitting moves the spin down $5d$ DOS toward the Fermi level, making the cubic structure unstable. As a result, the cubic $ErAl_2$ distorts into the lower symmetry rhombohedral structure. This is different from the tetragonal distortion in $PrAl_2$, which was shown to be only due to the $4f$ splitting [7]. Total energy calculations indeed confirm experimentally observed rhombohedral structure as the ground state of $ErAl_2$. This distortion is also associated with the crystallographic splitting of Al site in contrast to the tetragonal distortion of $PrAl_2$ where the Al atoms remain symmetrically equivalent.

13

It is interesting to note that the rhombohedral ErAl$_2$ has lower total energy compared to the tetragonal PrAl$_2$. However, the total energies of both the tetragonal (for the high concentration of Pr) and rhombohedral (for the high concentration of Er) structures increase for the x = 0.375, 0.5, and 0.625 in Pr$_{1-x}$Er$_x$Al$_2$ and, indeed, no structural distortion has been observed experimentally for x = 0.4.

Figure 10 shows crystal field energy (both 5d and 4f) and 5d exchange splitting as functions of Er content. Both trends match the experimentally observed decrease of the nuclear heat capacity coefficient with increase in x (Er). It is indeed well known that the nuclear heat capacity is high for the systems in which both the 4f crystal field interactions and conduction electron exchange splitting due to indirect 4f-4f exchange interactions are strong [26].

Unusual magnetism of Pr$_{1-x}$Er$_x$Al$_2$ for intermediate x can be connected with the neighboring Pr/Er interactions and anisotropic 4f energy landscapes; the latter are shown in Fig. 11 and where calculated from the anisotropic energy density relation

$\frac{E_a}{V} \approx \frac{\kappa_2}{2}\left(3\cos^2\theta - 1\right) + \frac{\kappa_4}{8}\left(35\cos^4\theta - 30\cos^2\theta + 3\right)$ [27, 28, 29], where κ_2 (second order)

and κ_4 (fourth order) coefficients are products of the corresponding quadrupolar/octupolar moments and crystal field parameters within the crystal environment. The mixed 4f energy density landscapes at high concentrations of Pr indicate easy axis magnetism, which at high concentrations of Er changes over to easy plane (see Ref. 30). The easy axis magnetism becomes unstable for x = 0.375, 0.5 and,

14

especially, x = 0.625, leading to instability due to nearly spherical energy density.

Further, instability that results from changing the sign of the anisotropy constant in these

compositions, leads to multiple magnetic transitions as a function of magnetic field seen

experimentally [13].

Figure 12 shows calculated FM and FIM magnetic moments as a function of Er content.

The FM moments are linearly increasing as expected. The FIM moments are lower than

FM moments (mainly for x = 0.375, 0.5, 0.625) due to the antiparallel alignment between

the Pr and Er moments indicating stronger effective Pr/Er interactions that may lead to

anomalous magnetic transformations as observed from the experiment. The FIM moment

determined from neutron diffraction for 0.6Pr/0.4Er indeed lies in this range (0.9 μ_B/R)

[13].

Every R atom in the $MgCu_2$-type Laves phase is surrounded by 4 nearest neighbor R

atoms at $\delta_{R-R} = a\sqrt{3}/4 \cong 3.4$ Å, 12 next near neighbor R atoms at $\delta_{R-R} = a/\sqrt{2} \cong 5.6$ Å, 12

third near neighbor R atoms at $\delta_{R-R} = a\sqrt{11}/4 \cong 6.6$ Å, and 6 fourth near neighbor R atoms

at $\delta_{R-R} = a \cong 7.9$ Å . In order to visualize the differences in the magnetic ordering in this

mixed-lanthanide system, one may use the effective magnetic surface potential (k-space

potential), $J(h)$. The latter can be expanded in a Fourier series limited to the first few

near neighbor magnetic exchange interaction parameters, $j(s)$, using a function $Y^{(s)}$,

i.e. $J(h) = \sum_s j(s)Y^{(s)}(h)$. Here, $Y^{(s)}$ given in Ref. [31] for an arbitrary coordination

shell, s, of the face centered cubic structure has been modified for the $MgCu_2$-type Laves phase structure.

Figure 13a illustrates effective magnetic surface potentials calculated from density functional theory (DFT), where $j(s)$ are negative for $s = 1, 3,$ and 4, but $j(s)$ is positive for $s = 2$ in $Pr_{0.625}Er_{0.375}Al_2$. Here, the second nearest neighbor exchange interactions [$j(2) = 12.5$ meV] are slightly weaker than the nearest neighbor ones [$j(1) = -13.6$ meV]; $j(3)$ and $j(4)$ are reduced by approximately one and two orders of magnitude, respectively, and therefore, are nearly negligible. The surface potential constructed using $j(1)$ through $j(4)$ from DFT depicted in Fig. 13a shows the development of peaks at k-points corresponding to all $j(s) > 0$, while simultaneously shifting the minima seen in the $j(s) < 0$ structure away from the ends of k-vectors [13]. The magnetic structure observed in a zero magnetic field in this mixed lanthanide compound may, therefore, become unstable leading to the Griffiths phase-like behavior in low magnetic fields and multiple metamagnetic transitions when the magnetic field is increased. Figure 13b shows effective magnetic surface potentials calculated for $x = 0.625$ ($Pr_{0.375}Er_{0.625}Al_2$) in which the second nearest neighbor exchange interactions are reduced by 30% compared to $j(2)$ of $x = 0.375$ (Fig. 13a). Similar behavior, i.e. reduction of $j(2)$ by 30%, has been found for lower Er content of $x = 0.125$ (Fig. 13c). Therefore, due to the reduced second nearest neighbor exchange interactions, the peaks indicating the short range FM behavior are diminished for concentrations both higher and lower than $x = 0.375$. This result is also supported by the calculated ferrimagnetic moment trend and the experimental results.

V. Summary

Heat capacity, magnetization measurements, and electronic structure calculations have been carried out in a mixed light (Pr) and heavy (Er) lanthanide $Pr_{1-x}Er_xAl_2$ system. Unlike in mixed heavy lanthanide dialuminides, the intermediate compositions in $Pr_{1-x}Er_xAl_2$ show anomalous magnetic behaviors such as short-range clustering, and metamagnetic transitions. Both $PrAl_2$ and $ErAl_2$ undergo crystallographic distortions at T_C, however, the underlying origins of these distortions are quite different, even though both compounds have same ground state magnetism. The $4f$ splitting is the main cause of tetragonal distortion in $PrAl_2$, but, unexpectedly, $5d$ crystal field is predominantly responsible for the rhombohedral distortion in $ErAl_2$. The interplay between the $4f$ and $5d$ crystal field splitting and $5d$ exchange splitting drives anomalous magnetic behaviors in the intermediate compositions of $Pr_{1-x}Er_xAl_2$. The easy axis and easy plane type anisotropic energy densities confirm tetragonal and rhombohedral distortions in $PrAl_2$ and $ErAl_2$, respectively. These energy density landscapes deviate from easy axis and easy plane type magnetization directions for $x = 0.375$, 0.5, and 0.625 suggesting no correlation with structural deformation but point to anomalous magnetic behaviors as observed from experiments. The magnetic surface potentials calculations show FIM $Pr_{0.625}Er_{0.375}Al_2$ in which the second nearest neighbor exchange interactions are opposite to the first nearest neighbor exchange interactions.
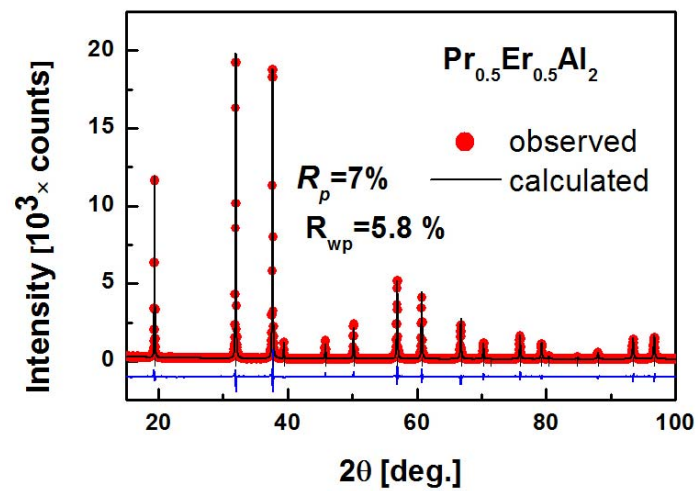
Acknowledgments

Fig. 1. Observed (symbols) and calculated (line drawn through the symbols) room temperature x-ray powder diffraction pattern of $Pr_{0.5}Er_{0.5}Al_2$; the bottom line represents the difference between the observed and calculated intensities.

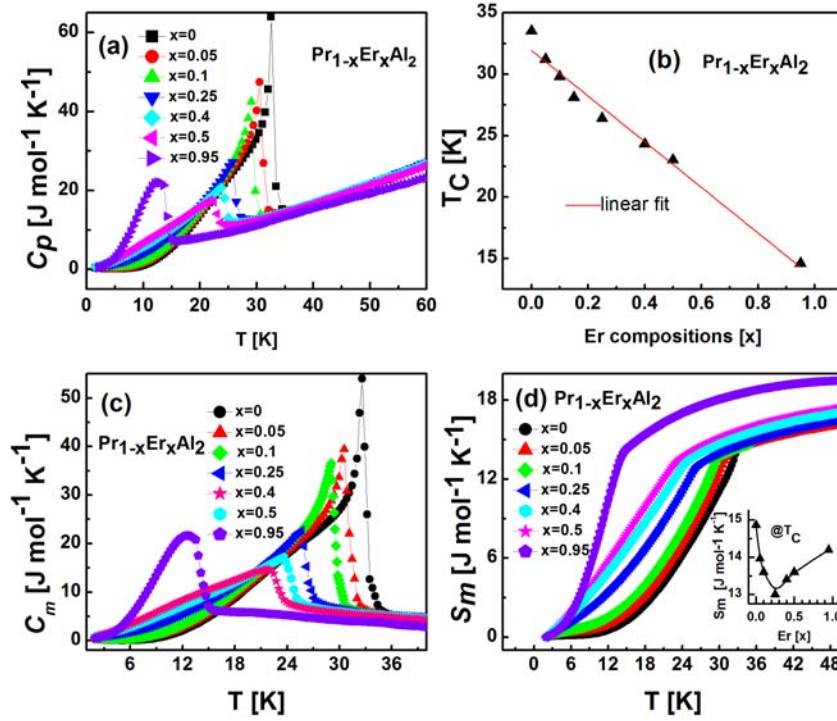**FIG. 2**. (a) Heat capacity C_p of $Pr_{1-x}Er_xAl_2$ measured in zero magnetic field. (b) Curie temperature T_C as a function of Er concentration. (c) Magnetic contribution to the heat capacity as a function of temperature for $Pr_{1-x}Er_xAl_2$ at zero magnetic field. (d) Magnetic entropy as a function of temperature for $Pr_{1-x}Er_xAl_2$ at zero magnetic field. Inset in (d) shows magnetic entropy at T_C as a function of Er concentration in $Pr_{1-x}Er_xAl_2$.
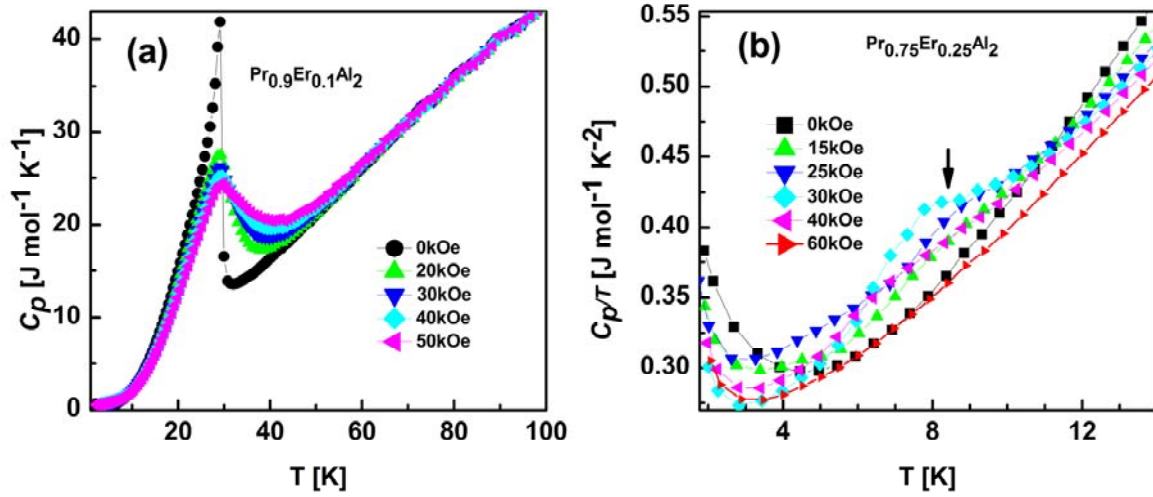
Fig. 3. Heat capacity C_p of $Pr_{0.9}Er_{0.1}Al_2$ measured in magnetic fields up to 50 kOe.

(b) C_p/T (T) for $Pr_{0.0.75}Er_{0.25}Al_2$ below T_C. In Fig. b, C_p was measured up to 300 K, only

C_p/T below T_C shown for clarity of field induced transition at T~8 K.
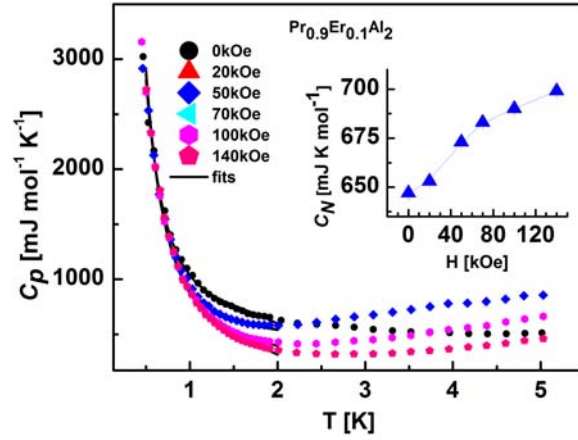
Fig. 4. Heat capacity C_p of $Pr_{0.9}Er_0$Heat capacity measured between 5 K and 360 mK for $Pr_{0.9}Er_{0.1}Al_2$ at magnetic fields up to 140 kOe. Inset shows nuclear heat capacity as a function of applied magnetic fields.
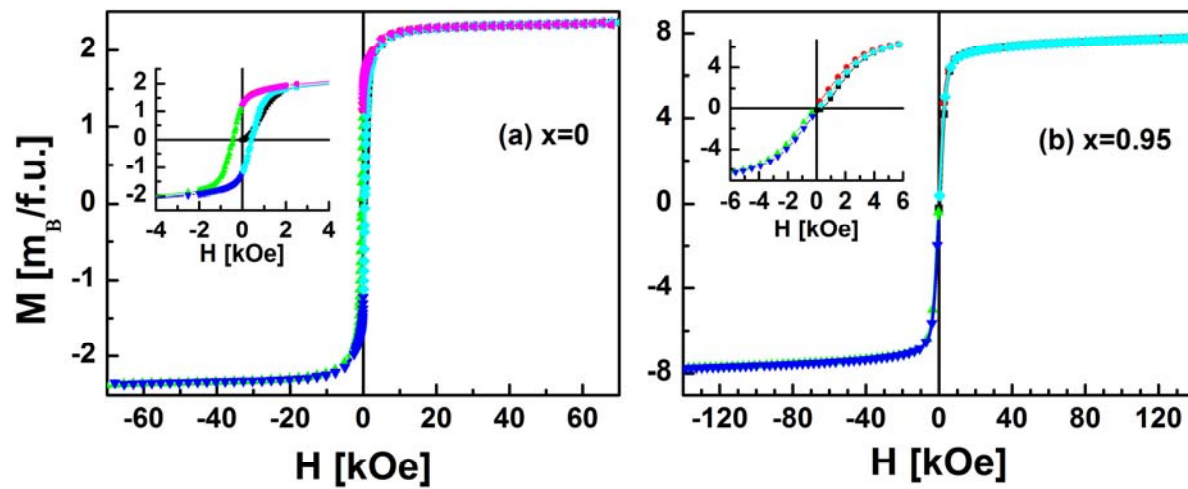
Fig. 5. Magnetization as function of applied magnetic field for (a) x = 0 and (b) x = 0.95.
The insets show details at low magnetic fields.
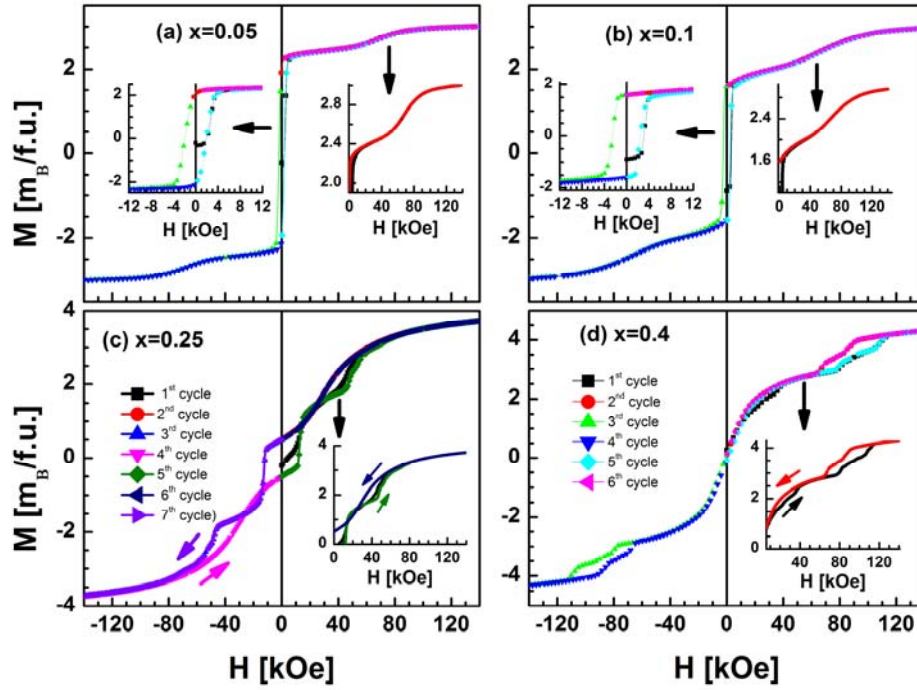
Fig. 6. Magnetization as function of applied magnetic field for (a) x = 0.05, (b) x = 0.1, (c) x = 0.25, and (d) x = 0.4. The insets show details of magnetization at low magnetic fields for x = 0.05 and 0.01, and provide closer picture of the high-field magnetization anomalies for all samples. The hysteresis loops were carried out as 0→140 (1st cycle)→ -140 (2nd, and 3rd cycle) →+140 (4th, and 5th cycle) →0 kOe (6th cycle).
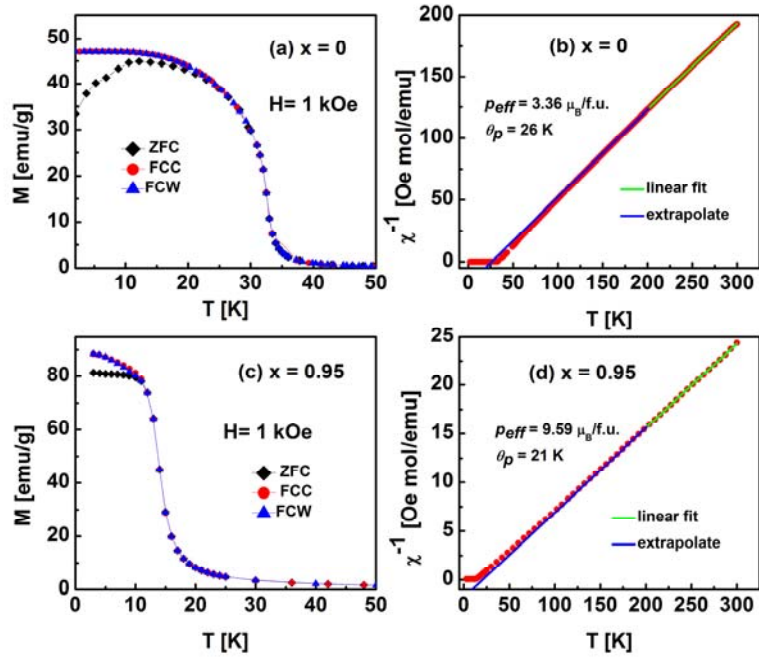
Fig. 7. Zero field cooled warming, field cooled cooling, and field cooled warming magnetization for (a) x = 0 and (c) x = 0.95 at H = 1 kOe. The inverse dc magnetic susceptibility χ^{-1} (T) as a function of temperature for (b) x = 0 and (d) x = 0.95 at H = 1 kOe.
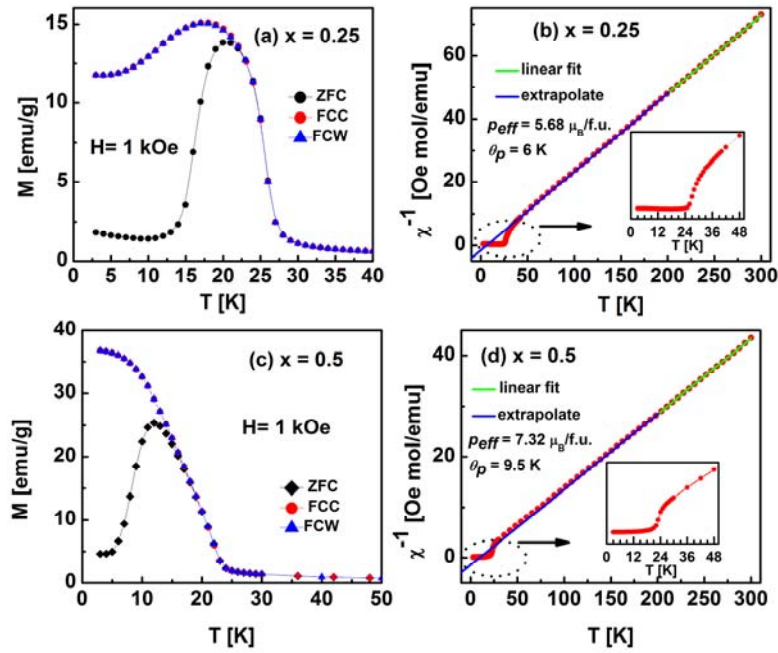
Fig. 8. Zero field cooled warming, field cooled cooling, and field cooled warming magnetization for (a) x = 0.25 and (c) x = 0.5 at H = 1kOe. The inverse dc magnetic susceptibility χ^{-1} (T) as a function of temperature for (b) x = 0.25 and (d) x = 0.5 at H = 1 kOe. The insets in (b) and (d) show low temperature χ^{-1} behavior at H = 1 kOe.
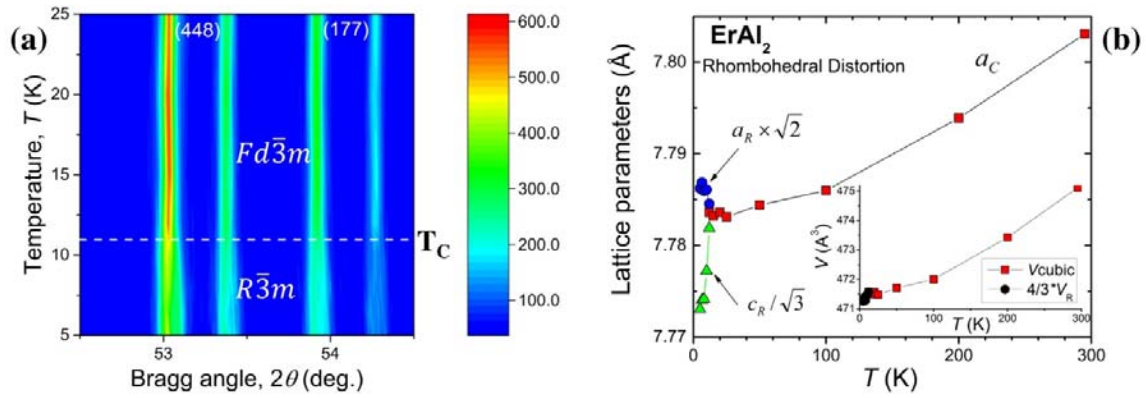
Fig. 9. (a) Contour plot of x-ray diffraction pattern of two high-angle Bragg reflections [(448) and (177)] of ErAl$_2$. b) Temperature dependence of the lattice parameters and unit-cell volume (inset) of ErAl$_2$ measured during cooling in zero magnetic field. The lattice parameters of the low-temperature rhombohedral phase are normalized for a comparison with the high-temperature cubic phase.
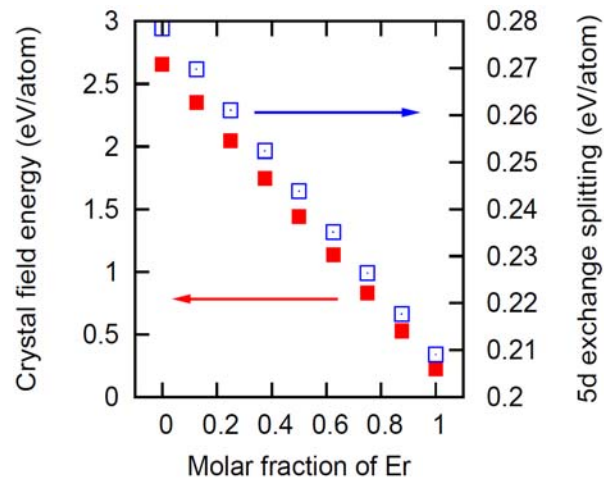
Fig. 10. Crystal field energy (energy required to split degenerate 4*f* states as well as 5*d* states). The 5*d* exchange splitting is the energy difference between the spin up and spin down 5*d* band centers.
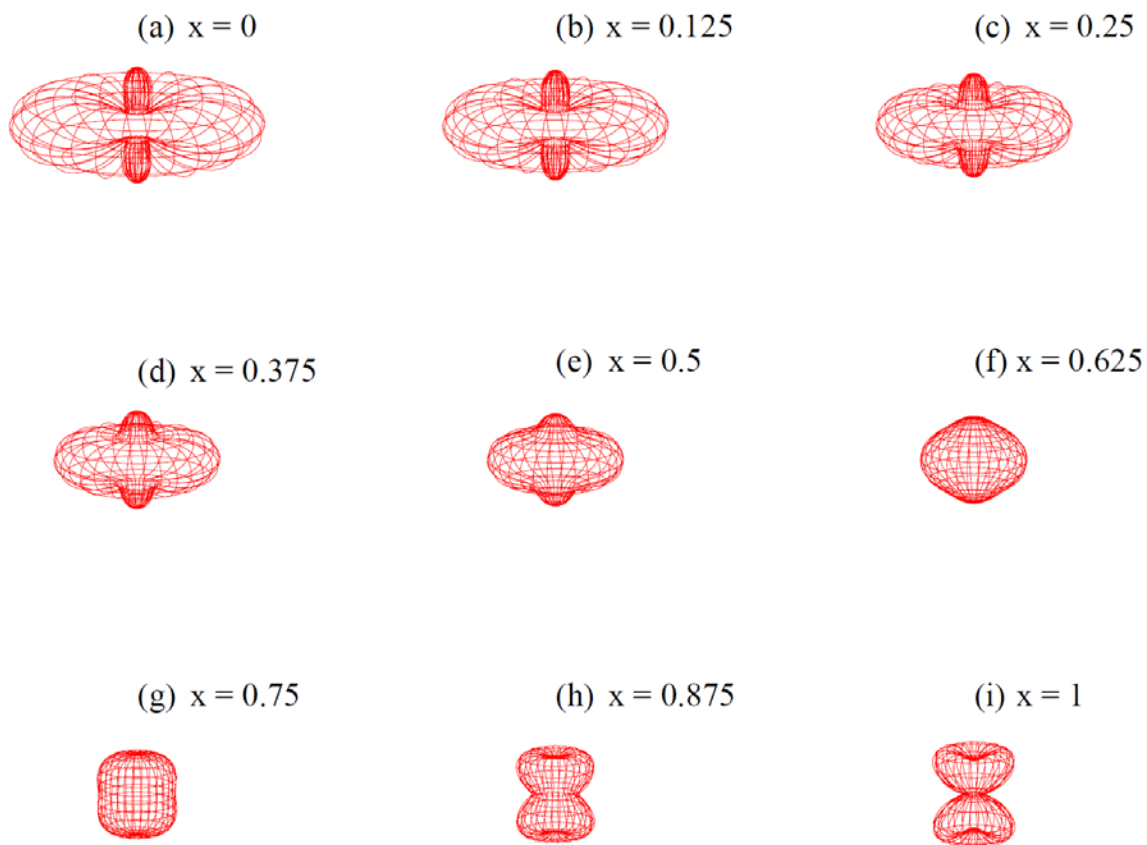
(a) x = 0 (b) x = 0.125 (c) x = 0.25

(d) x = 0.375 (e) x = 0.5 (f) x = 0.625

(g) x = 0.75 (h) x = 0.875 (i) x = 1

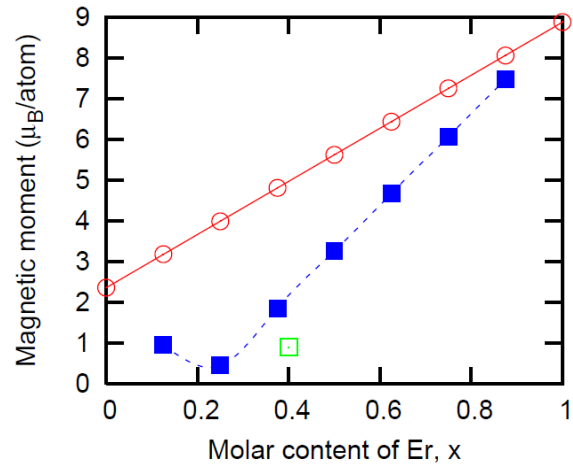**Fig. 11**. Anisotropic $4f$ energy density including the contributions from quadrupolar and octopolar moments of $Pr_{1-x}Er_xAl_2$.

Fig. 12. Calculated magnetic moments of FM (open circles) and FIM (filled squares) of $Pr_{1-x}Er_xAl_2$. The open square denotes FIM moment found from neutron experiment.

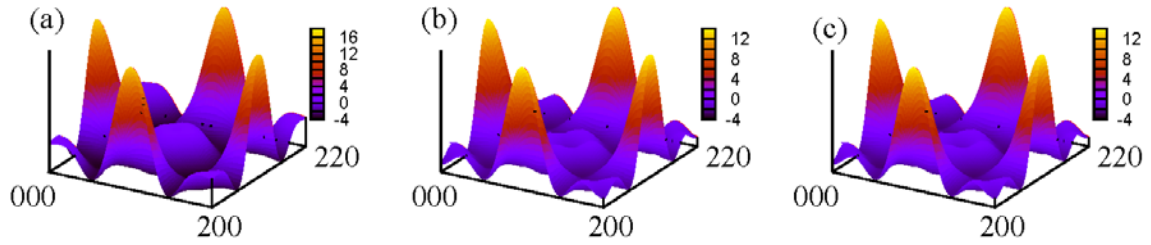**Fig. 13**. (a) The magnetic surface potentials of FIM for x = 0.375 in $Pr_{1-x}Er_xAl_2$. Here the second nearest neighbor exchange interactions [$j(2) = 12.5$ meV] are opposite to the first nearest neighbor exchange interactions [$j(1) = -13.6$ meV]. The effective magnetic surface potentials for x = 0.625 (b) and x = 0.125 (c) in which the second nearest neighbor exchange interactions are reduced by 30% compared to x = 0.375.

References:

[1] N. Jammalamadaka, N. Mohapatra, S. D. Das, and E. V. Sampathkumaran, Phys. Rev. B **79**, 060403(R) (2009).

[2] J. L. Wang, L. Caron, S. J. Campbell, S. J. Kennedy, M. Hofmann, Z. X. Cheng, M. F. Md Din, A. J. Studer, E. Brück, and S. X. Dou, Phys. Rev. Lett. **110**, 217211 (2013).

[3] K. Mukherjee, S. D. Das, N. Mohapatra, K. K. Iyer, and E. V. Sampathkumaran, Phys. Rev. B **81**, 184434 (2010).

[4] B. Maji, K. G. Suresh, and A. K. Nigam, App. Phys. Lett. **102**, 062406 (2013).

[5] S.-W. Han, C. H. Booth, E. D. Bauer, P. H. Huang, Y. Y. Chen, and J. M. Lawrence, Phys. Rev. Lett. **97,** 097204 (2006).

[6] H. Miyagawa and G. Oomi, M. Ohashi, I. Satoh, T. Komatsubara, M. Hedo, Y. Uwatoko, Phys. Rev. B **78**, 064403 (2008).

[7] A. K. Pathak, D. Paudyal, Ya. Mudryk, K. A. Gschneidner, Jr. and V. K. Pecharsky, Phys. Rev. Lett. **110**, 186405 (2013).

[8] M. Khan, D. L. Schlagel, T. A. Lograsso, K. A. Gschneidner, Jr., and V. K. Pecharsky, Phys. Rev. B **84**, 134424 (2011).

[9] A. L. Lima, K. A. Gschneidner, Jr., V. K. Pecharsky, and A. O. Pecharsky, Phys. Rev. B **68**, 134409 (2003).

[10] M. Khan, K. A. Gschneidner, Jr., and V. K. Pecharsky, Phys. Rev. B **80**, 224408 (2009).

[11] M. Khan, D. Paudyal, Y. Mudryk, K. A. Gschneidner, Jr., and V. K. Pecharsky Phys. Rev. B **83**, 134437 (2011).

[12] D. Paudyal, A. K. Pathak, V.K. Pecharsky, and K.A. Gschneidner, Jr., J. Phys.: Condens. Matter **25**, 396002 (2013).

[13] A. K. Pathak, D. Paudyal, W. T. Jayasekara, S. Calder, A. Kreyssig, A. I. Goldman, K. A. Gschneidner, Jr., and V. K. Pecharsky, Phys. Rev. B **89**, 224411 (2014).

[14] Materials Preparation Center, Ames Laboratory of US, DOE, Ames, IA, USA, www.mpc.ameslab.gov.

[15] A. P. Holm, V. K. Pecharsky, K. A. Gschneidner, Jr., R. Rink, and M. Jirmanus, Rev. Sci. Instrum. **75**, 1081 (2004).

[16] B. Hunter, Rietica-A Visual Rietveld Program, International Union of Crystallography Commission on Powder Diffraction Newsletter No. 20, (Summer, 1998) [http://www.rietica.org].

[17] V. K. Pecharsky, J. O. Moorman, and K. A. Gschneidner Jr., Rev. Sci. Instrum. **68**, 4196 (1997).

[18] V. I. Anisimov, F. Aryasetiawan, and A. I. Lichtenstein, J. Phys.: Condens. Matter. **9** 767 (1997).

[19] O. K. Andersen and O. Jepsen, Phys. Rev. Lett. **53** 2571(1984)

[20] P. Blaha, K. Schwarz, G. Madsen, D. Kvasnicka, and J Luitz, *WIEN2k*, An Augmented Plane Wave + Local Orbitals Program for Calculating Crystal Properties (Karlheinz Schwarz, Techn. Universität Wien, Austria), ISBN 3-9501031-1-2 (2001).

[21] C. Kittel, *Introduction to Solid State Physics* (Wiley, New York), 8th ed. (2005).

[22] A. K. Pathak, K. A. Gschneidner, Jr., and V. K. Pecharsky, J. Appl. Phys. **117**, 17C107 (2015).

[23] C. Magen, P. A. Algarabel, L. Morellon, J. P. Araújo, C. Ritter, M. R. Ibarra, A. M. Pereira, and J. B. Sousa , Phys. Rev. Lett. **96**, 167201 (2006).

[24] S. Guo, D. P. Young, R. T. Macaluso, D. A. Browne, N. L. Henderson, J. Y. Chan, L. L. Henry and J. F. DiTusa, Phys. Rev. Lett. **100**, 017209 (2008).

[25] U. Kobler, and A. Hoser, J. Magn. Magn. Mat. **299**, 145 (2016).

[26] J. Jensen and A. R. Mackintosh, Rare earth magnetism: structures and excitations, Clarendon Press, Oxford, (chapter 7), (1991).

[27] R. Skomski, Simple Models of Magnetism (Oxford: Oxford University Press) p 79 chapter 3 (2006) and references therein.

[28] A. J. Freeman and R. E. Watson, Phys. Rev. **127**, 2058 (1962).

[29] P. Fulde, Crystal Fields in *Hand Book on the Physics and Chemistry of Rare Earths*. eds Gschneidner, Jr, KA, Eyring L (North-Holland, Amsterdam, New York, Oxford), Vol. **2**, p. 295 (1979).

[30] R. Skomski, Simple Models of Magnetism (Oxford: Oxford University Press) p 79 chapter 3 (2006) and references therein.

[31] D. de Fontaine, *Solid State Physics*, edited by H. Ehrenreich, F. Seitz, D. Turnbull (Academic Press, New York, San Frannsico, London), Vol. **34**, p.73. (1979).